Astron. Astrophys. 357, 51–60 (2000)

ASTRONOMY AND ASTROPHYSICS

High-redshift quasars lensed by spiral galaxies

M. Bartelmann

Max-Planck-Institut für Astrophysik, P.O. Box 1523, 85740 Garching, Germany

Received 8 September 1999 / Accepted 2 March 2000

Abstract. Given its extraordinary spatial resolution and sensitivity, the projected Next Generation Space Telescope (NGST) is likely to detect a large number of high-redshift QSOs lensed by spiral galaxies. Using realistic models for the QSO and spiral populations, we calculate the expected number density of detectable QSOs multiply imaged by spirals, and investigate the influence of various evolution effects on that number density. It is shown that NGST will probably find of order ten lensed QSOs per square degree at 26th magnitude in the V and L bands, and that various observable quantities like the total number density of lensed QSOs in these two bands, the ratio between the number densities of lensed QSOs in the V and L bands, the fraction of QSOs with more than two images and so forth can be used to constrain the evolution of the QSOs, the spirals, the dust in spirals, and the masses of spiral disks.

Key words: galaxies: spiral – galaxies: quasars: general – cosmology: gravitational lensing

1. Introduction

Strong gravitational lensing of QSOs is predominantly caused by elliptical rather than spiral galaxies. Although the majority of galaxies are spirals, they are only about half as massive as ellipticals and are therefore substantially weaker lenses (e.g. Turner et al. 1984; Fukugita & Turner 1991; Maoz & Rix 1993; Kochanek 1996a,b; Keeton et al. 1997; Falco et al. 1998; Keeton et al. 1998). A few known QSOs, however, are lensed by spiral galaxies, and a number of recent papers investigated the question of how the disks in spirals influence lensing cross sections (Maller et al. 1997; Keeton & Kochanek 1998; Bartelmann & Loeb 1998; Blain et al. 1999). If observations at high angular resolution can be combined with high sensitivity, numerous QSOs multiply imaged by spiral galaxies can be expected to be observed, and such observations can provide detailed information on the evolution of spiral galaxies and their properties out to fairly high redshift.

This paper addresses the question of how many QSOs lensed by spiral galaxies can be expected to be observed by telescopes like NGST, whose angular resolution exceeds $0.1''$, and which reach a sensitivity of order one nano-Jansky in the visible and near-infrared wave bands. Going to such observational limits, QSOs lensed by spiral galaxies should be discovered in substantial numbers. Many of the multiple-image systems produced by spiral galaxies will straddle near-edge-on galactic disks. The statistics of image separations and time delays will therefore allow to determine properties of spiral disks at moderate and high redshifts. The wavelength regime between the visible and the near infrared is particularly interesting for such investigations, since the importance of dust changes dramatically across this wavelength range. While multiple QSO images, in particular near galactic disks, are substantially obscured by dust in the V band, they are almost unaffected in the L band. Comparing observations taken in these two wavebands, it will therefore be possible to quantify the amount and the distribution of dust in distant spiral disks.

The very faint flux limits envisaged will bring high-redshift QSOs into view. The QSO population at high redshifts is uncertain. Observations show a quick drop of the QSO number density beyond redshifts of $4-5$ (Pei 1995). This may reflect rapid QSO evolution at these redshifts, but also incompleteness of the QSO samples observed. We therefore investigate two alternatives, assuming either that the observed QSO population is complete, or that it is to be extrapolated towards high redshifts.

It is also important for this study to reliably estimate QSO K-corrections in the visible and the near infrared. For this purpose, we model the dominant features of QSO spectra together with the Lyman-α forest, and determine K-corrections by convolving the redshifted model spectrum with the appropriate filter functions.

Finally, the contribution of disks to lensing by spiral galaxies is crucial for two reasons. First, projected disks at large inclination angles reach high surface mass densities and affect multiple-imaging cross sections substantially. Second, dust in these disks demagnifies images and thereby alters the statistics of observed image properties.

We proceed in the following way. Sect. 2 describes the computation of QSO K-corrections and summarises the model for the QSO luminosity function. Our model for the spiral galaxies is introduced in Sect. 3. Sect. 4 briefly describes the numerical method. Sect. 5 presents the results, and we finish with the conclusions in Sect. 6.

Send offprint requests to: Matthias Bartelmann (mbartelmann@mpa-garching.mpg.de)

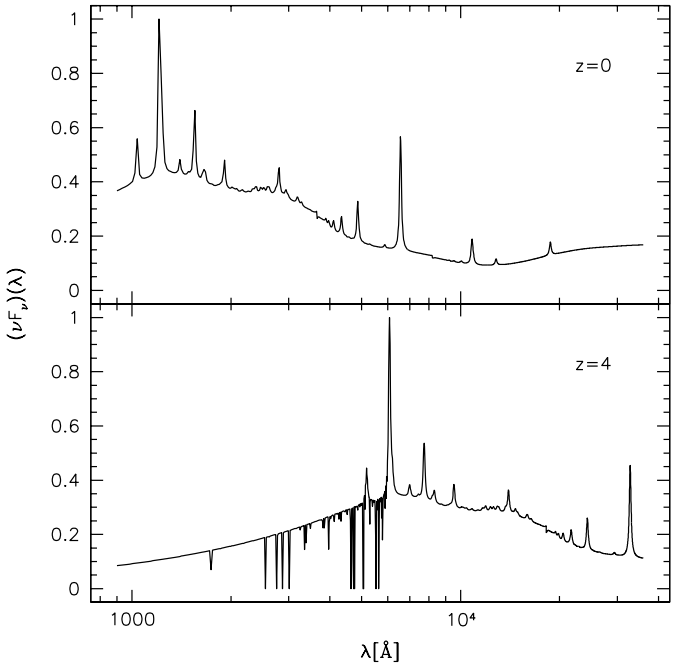

Fig. 1. Synthetic QSO spectra at redshifts $z = 0$ and $z = 4$ (top and bottom panel, respectively), including strong Lyman-α forest lines. Wavelengths range from 900 Å to $36,000$ Å. The ordinate is scaled to arbitrary units. The most prominent line in both spectra is Lyman-α.

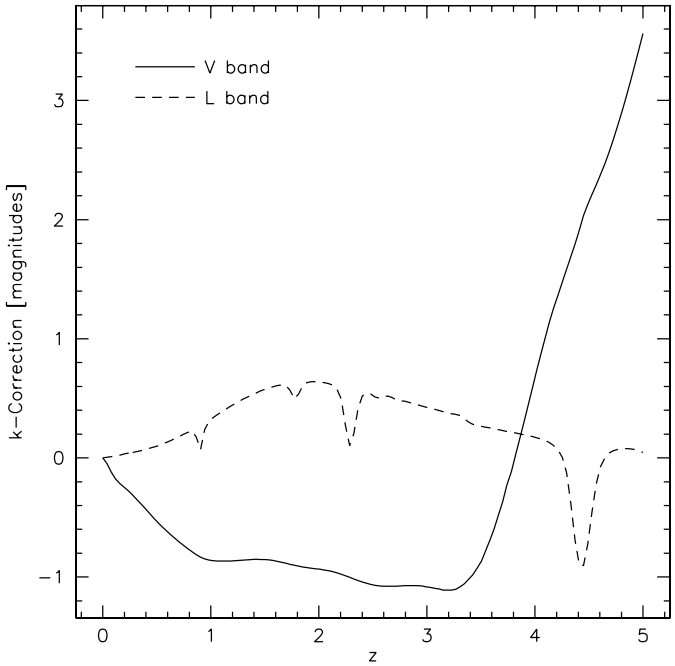

Fig. 2. K-corrections as functions of QSO redshifts in the V and L bands (solid and dashed lines, respectively), computed from synthetic QSO spectra convolved with the V and L response functions.

Throughout, we adopt a CDM cosmological model with $\Omega = 0.3$, $\Omega_\Lambda = 0$, and a Hubble constant of $H_0 = 70\,\mathrm{km\,s^{-1}\,Mpc^{-1}}$. The CDM spectrum is normalised such that the local abundance of rich galaxy clusters is reproduced (Eke et al. 1996; Viana & Liddle 1996).

2. QSOs

2.1. QSO spectra and the K-correction

A reliable estimate for the QSO K-correction is very important for the present study. We therefore have to construct a synthetic QSO spectrum representing the prominent features of a typical QSO spectrum. This spectrum consists of the underlying QSO continuum, the hydrogen emission lines of the Lyman, Balmer, and Paschen series, the corresponding Balmer and Paschen continua, the two-photon continuum, the 3000 Å bump mainly contributed by iron (Fe II) emission lines, and emission lines of several other elements like helium, carbon, nitrogen, oxygen and so forth.

We adopt the QSO continuum emission from Elvis et al. (1994), who tabulate the median QSO continuum in the frequency range $10^9\,\mathrm{Hz} \le \nu \le 10^{19}\,\mathrm{Hz}$. The spectrum on top of the broad continuum is modelled as in Grandi (1981, 1982). It contains the Balmer- and Paschen series up to order 28 with line strengths adopted from Brocklehurst (1971), exponential Balmer- and Paschen continua, the two-photon continuum as given by Spitzer & Greenstein (1951), 79 emission lines of Fe II to reproduce the 3000 Å bump, and several other emission lines of helium, carbon, nitrogen, oxygen, magnesium, and silicon. The electron temperature is assumed to be $12,500\,K$, the electron density is $10^6\,\mathrm{cm^{-3}}$, and the lines are broadened by Lorentzian profiles with an FWHM velocity of $4,500\,\mathrm{km\,s^{-1}}$. Some additional lines tabulated by Netzer & Davidson (1979) are added. Following Grandi (1982), the emission lines are normalised such that the equivalent width of the Hβ line against the continuum is 100 Å. Finally, the number density and equivalent widths of Lyman-α forest lines are modelled following Murdoch et al. (1986). A synthetic spectrum of a QSO at redshift $z = 4$ obtained in this way is displayed in Fig. (1).

The synthetic QSO spectrum is then convolved with the response functions of the Johnson V and L bands to obtain the K-correction. The peak transmission wavelengths of the response curves are at $0.555\,\mu\mathrm{m}$ for the V band and at $3.6\,\mu\mathrm{m}$ for the L band. The K-corrections in these bands are plotted in Fig. (2).

The K-correction in the V band is negative from redshift zero to just above redshift 3, where it rises steeply. Negative K-corrections are due to bright emission lines moving into the V-band response function, while the steep increase is caused by Lyman-α forest absorption. In the L band, the K-correction ranges between ± 1 magnitudes. The shallow peak in the L-band K-correction is due to the shallow valley in the QSO spectrum beyond $\approx 8,000$ Å. The pronounced minimum at $z \approx 4.4$ is caused by the Balmer-α line's coming into the L-band response function.

2.2. QSO luminosity function at high redshift

Haiman & Loeb (1998) recently provided a model for the QSO luminosity function at high redshifts. The model rests on four

simple and intuitive assumptions: (i) black holes form in all dark-matter haloes above a mass limit M_0; (ii) the black-hole mass $M_{\rm bh}$ is a certain constant small fraction ϵ of the halo mass; (iii) black holes produce QSOs shining at the Eddington luminosity $L_{\rm edd} = L_{\rm edd,\odot}\,M_{\rm bh}/M_\odot$ at birth, and the QSO luminosity is on average a monotonically decreasing function $M_{\rm bh}\,f(t)$ of time t after birth; and (iv) the mass function of dark-matter haloes is given by the Press-Schechter (1974) mass function $N(M)$.

The QSO luminosity function is then

$$\Phi(L,z) = \int_\infty^z {\rm d}z' \int_{M_0}^\infty {\rm d}M\,\frac{{\rm d}N(M)}{{\rm d}z'}\,\delta[L - M_{\rm bh}f(t)]\;. \quad (1)$$

The derivative of the Press-Schechter mass function with respect to z gives the birth rate of haloes and thus the birth rate of black holes, and the delta function selects those QSOs shining with luminosity L at time t after their birth.

The redshift derivative of the Press-Schechter mass function contains a negative contribution because of halo merging. It therefore underestimates the halo formation rate. However, the merger probability at high redshift is low, so that the underestimate is unimportant (see also Sasaki 1994).

The black-hole mass fraction ϵ is kept constant here for simplicity. Introducing a moderate scatter in ϵ (cf. Magorrian et al. 1998; Van der Marel 1999) affects the black-hole mass function only weakly (Haiman & Loeb 1999).

Haiman & Loeb used an exponential function for $f(t)$ and assumed $M_0 = 10^8\,M_\odot\,[(1+z)/10]^{-3/2}$ for the minimum halo mass. The model has then only two free parameters, the black-hole mass fraction ϵ and the time constant t_0 of $f(t)$. Haiman & Loeb showed that $\epsilon \approx 5.4\times10^{-3}$ and $t_0 \approx 6.3\times10^5\,{\rm yr}$ provide an excellent fit to the observed QSO luminosity function at intermediate redshifts (Pei 1995).

Carrying out the redshift integral in (1) leads to

$$\Phi(L,z) = \int_{M_0}^\infty \frac{{\rm d}M}{M|\dot f(t)|_{t_*}}\,\left.\frac{{\rm d}N(M)}{{\rm d}z}\right|_{z_*}\,\left.\frac{{\rm d}z}{{\rm d}t}\right|_{z_*}\;. \quad (2)$$

Here, z_* is the redshift at which a QSO in a halo of mass M needs to be born in order to reach luminosity L at redshift z, and t_* is the time elapsed between z_* and z. Note that another mass limit on the haloes is implicit here. The QSO cannot shine with higher than Eddington luminosity. The halo mass therefore needs to exceed both M_0 and $(M_\odot/\epsilon)\,(L/L_{\rm edd,\odot})$.

We repeat the derivation of Haiman & Loeb's luminosity function here because numerical evaluation reveals that sufficient approximations can be made to render the remaining integral in (2) analytically tractable. This is convenient because the accurate numerical evaluation of (2) requires substantial care because of the large dynamic range of the Press-Schechter mass function.

We introduce two approximations. The first is that t_* is typically very short compared to the Hubble time, so that $z_* \approx z$ is a very good approximation. The second is that the power spectrum $P(k)$ of the dark-matter density fluctuations can be written as a power law,

$$P(k) \propto k^n\;. \quad (3)$$

This approximation is well satisfied in the range of scales k corresponding to the relevant dark-matter halo masses, where $n \approx -2.4$. The first approximation removes the necessity to numerically evaluate z_*. The second approximation allows to write the Press-Schechter mass function as

$$N(M) = \frac{\bar\rho}{M_*^2}\,\left(\frac{2}{\pi}\right)^{1/2}\,\frac{\alpha}{D(a)}\,m^{\alpha-2}\,\exp\left(-\frac{m^{2\alpha}}{D^2(a)}\right)\;, \quad (4)$$

where $\bar\rho$ is the mean cosmic density *today*, M_* is the nonlinear mass scale *today*, $m \equiv M/M_*$ is the halo mass in units of M_*, $D(a)$ is the growth factor of density perturbations as a function of the scale factor a, and α is related to n through

$$\alpha \equiv \frac{n+3}{6}\;. \quad (5)$$

With (4), the remaining mass integral in (2) can be carried out. The final result for the luminosity function is

$$\Phi(L,z) = \frac{t_0}{L}\,\frac{{\rm d}z}{{\rm d}t}\,\frac{\bar\rho}{M_*}\,\frac{2^\beta}{\sqrt{2\pi}}\,a^2D'(a)D^{2\beta-2}(a) \times[2\Gamma(1+\beta,\mu_0) - \Gamma(\beta,\mu_0)]\;, \quad (6)$$

where we introduced the abbreviations

$$\beta \equiv \frac{\alpha-1}{2\alpha} \quad (7)$$

and

$$\mu \equiv \frac{m^{2\alpha}}{2D^2(a)}\;. \quad (8)$$

As mentioned before, μ_0 is determined through (8) by

$$M_0 = \max\left(M_0, \frac{LM_\odot}{L_{\rm edd,\odot}\epsilon}\right) \quad (9)$$

and $m \equiv M/M_*$. For low QSO luminosities, the term in brackets in (6) is constant in luminosity, and $\Phi(L,z) \propto L^{-1}$.

For $n = -2.4$, $\alpha = 0.1$ and $\beta = -4.5$. In an Einstein-de Sitter universe, $D(a) = a$ and ${\rm d}z/{\rm d}t = H_0\,a^{-5/2}$, and thus

$$\Phi(L,z) = \frac{t_0H_0}{L}\,\frac{\bar\rho}{M_*}\,\frac{2^\beta}{\sqrt{2\pi}}\,a^{2\beta-5/2} \times[2\Gamma(1+\beta,\mu_0) - \Gamma(\beta,\mu_0)]\;. \quad (10)$$

Eq. (10) shows that the QSO luminosity function $\Phi(L,z)$ is a very steep function of redshift. Ignoring the redshift dependence of M_0, $\Phi(L,z)$ scales with a approximately as $a^{-23/2}$, strongly depending on the local slope of the dark-matter power spectrum.

2.3. QSO number counts

Haiman & Loeb's model is valid at high redshifts. At low redshifts, the QSO luminosity function can be assumed to be sufficiently well observed. In order to test the impact of the theoretical extrapolation on the expected counts of strongly lensed QSOs, we use two alternative QSO luminosity functions, namely either Pei's (1995) fit to the observed QSO number counts alone, or Pei's function augmented by Haiman & Loeb's

(1998) theoretical model. In the latter case, we construct the luminosity function $\Phi(L,z)$ from the observed function out to redshift 3, from the theoretical model beyond redshift 4, and from a redshift-dependent linear combination of the two between redshifts 3 and 4. For simplicity, we shall refer to these two luminosity functions as the "observed" and the "theoretically extrapolated" one below.

Using the K-correction derived in Sect. 2.1, the QSO luminosity function can now be converted to number counts per flux and redshift intervals $\mathrm{d}S$ and $\mathrm{d}z$,

$$\frac{\mathrm{d}^2N(S,z)}{\mathrm{d}S\mathrm{d}z}\,\mathrm{d}S\mathrm{d}z\;. \tag{11}$$

3. Spiral galaxies

3.1. Evolution of spirals

We assume that the spiral population has a Schechter (1976) luminosity function, i.e. the number density n follows

$$\frac{\mathrm{d}n(l)}{\mathrm{d}l} = n_*\,l^\nu\,\exp(-l)\;, \tag{12}$$

where $l = L/L_*$ is the luminosity in units of L_*, $n_* = 1.5\times10^{-2}\,h^3\,\mathrm{Mpc}^{-3}$ is the present-day number density, and $\nu=-0.81$ (Marzke et al. 1994). We further assume that the circular velocity scales with l according to the Tully-Fisher (1977) relation,

$$\frac{v_\mathrm{c}}{v_{\mathrm{c}*}} = l^{1/\alpha}\;, \tag{13}$$

with $\alpha=4$. We adopt two scenarios for the redshift evolution of the spiral population, namely either constant comoving number density, or a number density evolving according to the Press-Schechter mass function.

Mo et al. (1998) suggested a model for the evolution of spiral disks resting upon four simple and intuitive assumptions. These are: (i,ii) The disk mass and angular momentum are fixed fractions of the spiral mass and angular momentum. (iii) The radial disk profile is exponential, and the disk is centrifugally supported. (iv) The disk is dynamically stable.

These assumptions yield a set of simple scaling relations for the disk properties. Disk mass $M_\mathrm{d}(z)$ and radius $r_\mathrm{d}(z)$ scale with the inverse Hubble parameter $H(z)$,

$$(M,r)_\mathrm{d} \propto \left[\frac{H(z)}{H_0}\right]^{-1}\;, \tag{14}$$

and consequently the disk surface mass density $\Sigma_\mathrm{d}(z)$ scales with the Hubble parameter,

$$\Sigma_\mathrm{d}(z) \propto \frac{H(z)}{H_0}\;. \tag{15}$$

We use either constant disk parameters below or evolve them according to Eqs. (14) and (15).

Finally, we assume that the disk radius r_d scales with luminosity as

$$r_\mathrm{d} \propto l^{1/2}\;. \tag{16}$$

3.2. The lens model

Our mass model for the spirals consists of two components, a halo and a disk. They are modelled as described in Keeton & Kochanek (1998) and Bartelmann & Loeb (1998). We refer the reader to these papers for details. In essence, both components are described as isothermal, arbitrarily flattened, ellipsoidal mass distributions, characterised by a core radius s and an oblateness q, defined as the ratio between the short and the long axes of an oblate ellipsoid. We can then compose the lensing potential ψ of a spiral with a maximal disk of three building blocks,

$$\psi_\mathrm{max} = \psi(s_\mathrm{d},q_\mathrm{d}) - \psi(r_\mathrm{d},q_\mathrm{d}) + \psi(s_\mathrm{h},1)\;. \tag{17}$$

The first two terms are the lensing potential of the disk, truncated at radius r_d, the third is the lensing potential of the halo. For sub-maximal disks with a disk fraction $0\le f_\mathrm{d}\le 1$, this is changed to

$$\psi = f_\mathrm{d}\,\psi_\mathrm{max} + (1-f_\mathrm{d})\,\psi(s_\mathrm{h},1)\;, \tag{18}$$

i.e. the truncated maximal-disk model is scaled down by f_d and embedded in a spherical halo of unchanged mass. We therefore have five parameters in total for the mass model, namely the core radius of the disk s_d, the core radius of the halo s_h, the oblateness of the disk q_d, the disk fraction f_d, and the asymptotic circular velocity v_c.

For an L_* galaxy, we assume a circular velocity of $v_{\mathrm{c}*} = 220\,\mathrm{km\,s}^{-1}$ and a disk radius of $r_{\mathrm{d}*} = 8\,h^{-1}$ kpc. They scale with spiral luminosity as given by Eqs. (13) and (16).

Flat rotation curves require a halo core radius of $s_\mathrm{h}\approx 0.72\,r_\mathrm{d}$ (Keeton & Kochanek 1998), and for the disk core radius we assume $s_\mathrm{d} = 0.2\,h^{-1}$ kpc. The disk fraction is either set to 1 or 0.5.

Up to a constant, the light travel time to the observer from a source at angular position $\boldsymbol{\beta}$ through an image position $\boldsymbol{\theta}$ is given by

$$t(\boldsymbol{\theta}) = \frac{1+z'}{c}\,\frac{D(z')D(z)}{D(z',z)}\,\left[\frac{1}{2}(\boldsymbol{\theta}-\boldsymbol{\beta})^2 - \psi(\boldsymbol{\theta})\right]\;, \tag{19}$$

where z' and z are the lens and source redshifts, respectively; $D(z',z)$ is the angular-diameter distance between redshifts z' and z, and $D(z)\equiv D(0,z)$. The lens equation relates $\boldsymbol{\theta}$ and $\boldsymbol{\beta}$ through

$$\boldsymbol{\beta} = \boldsymbol{\theta} - \boldsymbol{\alpha}(\boldsymbol{\theta})\;, \tag{20}$$

where $\boldsymbol{\alpha}(\boldsymbol{\theta}) = \nabla\psi(\boldsymbol{\theta})$ is the deflection angle. The time delay between images is therefore determined by the lensing potential, its gradient, and the geometry of the lens system.

3.3. Gas and dust

The disk is further assumed to encompass a double-exponential neutral-hydrogen disk with a scale radius given by r_d, a scale height of $q_\mathrm{d}r_\mathrm{d}$, and a central column density of $11.25\times10^{20}\,\mathrm{cm}^{-2}$ (Broeils & van Woerden 1994). Dust follows the

neutral-hydrogen distribution with a present-day dust-to-gas ratio of 0.01 (Whittet 1992). The dust is assumed to be a mixture of silicates and graphites, for which the extinction curve as a function of wavelength was derived by Draine & Lee (1984). The dust-to-gas ratio is either assumed to be constant with redshift, or to evolve in proportion to $(1+z)^{-2}$ (Pei et al. 1991).

3.4. Summary of the spiral model

Having fixed the disk radius, the disk core radius, the halo core radius, and the asymptotic circular velocity, and assuming the scalings of the circular velocity and the disk radius with luminosity, the mass model for the spirals has two more free parameters, namely the disk fraction f_d and the disk oblateness q_d.

The number density of spirals is then either assumed to be constant or to evolve according to the redshift evolution of the Press-Schechter mass function in the appropriate mass range. The parameters of individual spirals are either assumed to be constant with redshift, or to evolve according to the model by Mo et al. (1998). The dust-to-gas ratio in the spiral disks finally is either assumed to be constant or to evolve proportional to $(1+z)^{-2}$.

We focus on a fiducial model with disk oblateness $q_\mathrm{d}=0.2$, disk fraction $f_\mathrm{d}=1$, and evolving disk parameters, number density, and dust.

3.5. Visibility of faint QSO images

Many QSO images lensed by spiral galaxies will appear close to spiral disks. In order to be detectable, they need to be sufficiently brighter than the disk itself. We can estimate a maximum QSO magnitude in the following way. Freeman's (1970) law asserts that the central surface brightness of nearby spirals is $\approx 21.5\,\mathrm{mag\,arcsec^{-2}}$ in the B band. At redshift $z=0.6$, the surface brightness is cosmologically reduced by a factor $(1+z)^{-4}=0.15$, or $\approx 2\,$mag. The K-correction in the B band for an Sc galaxy at redshift 0.6 is $\approx 1\,$mag (Coleman et al. 1980; Rocca-Volmerange & Guiderdoni 1988). Schade et al. (1996) find that the B-band surface brightness of field spirals is $\approx 1\,$mag higher than expected from extrapolating Freeman's law to redshift 0.6. Taking cosmological dimming, K-correction and brightening together, the B-band surface brightness at redshift 0.6 is expected to be $\approx 23.5\,\mathrm{mag\,arcsec^{-2}}$. An Sc spiral at that redshift has $(\mathrm{B}-\mathrm{V})\approx 0.6$ (Guiderdoni & Rocca-Volmerange 1988). Assuming that typical scale lengths are equal in the B and V bands, the V-band surface brightness at $z=0.6$ is $I_{0,\mathrm{V}}(0.6)\approx 22.9\,\mathrm{mag\,arcsec^{-2}}$.

Typical image separations from the lens centre are of order the Einstein radius, or roughly $1\,h^{-1}\,\mathrm{kpc}$. Assuming an exponential light profile with a scale length of $\approx 3\,h^{-1}\,\mathrm{kpc}$ (Schade et al. 1996), the disk surface brightness near image locations has dropped by a factor of ≈ 0.7 to $I_\mathrm{V}(0.6)\approx 23.2\,\mathrm{mag\,arcsec^{-2}}$.

NGST is planned to achieve an angular resolution of $0.06''$. The V-band disk brightness in a circle of that diameter is therefore of order $29\,$mag. Hence, it seems realistic to expect that QSO images brighter than $\approx 28\,$mag can safely be detected on top of a spiral disk at redshift $\approx 0.5-0.6$. We restrict the computation of imaging probabilities below to multiple images with a maximum flux ratio of 20, or a magnitude difference of $3\,$mag. In the worst case of a QSO image pair on top of a spiral disk, the brighter image therefore has to have $\approx 25\,$mag for the fainter image to be seen. However, many multiple QSO images will straddle near-edge-on disks, whose surface brightness drops rapidly away from their symmetry line. On the whole, we can assume that QSO image systems with a total brightness $\lesssim 26\,$mag can be detected as multiple images against the brightness of the lensing disks.

This estimate applies to the V band. Spiral disks are brighter in the near infrared, where QSOs are intrinsically fainter. However, QSO host galaxies are substantially more prominent in the near infrared and give rise to characteristic lensing features like arcs and rings (Kochanek et al. 1999), which help in detecting lensed QSOs against spiral disks, and in distinguishing them from surface-brightness fluctuations. In addition, spiral disks are more concentrated in the near infrared, so that their light falls off more rapidly towards the locations of lensed QSO images.

Confusion of the images with bright spots of stellar appearance like OB associations or other surface-brightness fluctuations can also be disentangled through colour information or highly resolved X-ray observations. The order of magnitude of the previous estimate should therefore also hold in the L band.

4. Method of computation

We wish to compute the number of QSOs above a certain flux limit S lensed by spiral galaxies such that the images have certain properties Q. Let

$$\frac{\mathrm{d}^2N(S,z)}{\mathrm{d}S\mathrm{d}z}\mathrm{d}S\mathrm{d}z \tag{21}$$

be the number of unlensed quasars with flux within $\mathrm{d}S$ of S and redshift within $\mathrm{d}z$ of z. Let further $P(\mu,z;Q)$ be the probability for a quasar at redshift z to be magnified by a factor $\geq\mu$ and lensed with image properties Q. The number of lensed quasars in the redshift interval $z_1\leq z\leq z_2$ above the flux limit S is then

$$N(S)=\int_0^\infty\mathrm{d}S'\int_{z_1}^{z_2}\mathrm{d}z\,P\left(\frac{S}{S'},z;Q\right)\left[\frac{\mathrm{d}^2N(S,z)}{\mathrm{d}S\mathrm{d}z}\right](S',z). \tag{22}$$

The lensing probability $P(\mu,z;Q)$ is conveniently computed in the cross-section approach. The cross section $\sigma(\mu,z',z,l;Q)$ is defined as the area on the source sphere at redshift z in which a source must fall in order to be lensed with image properties Q and magnified by $\geq\mu$ by an individual galaxy with luminosity lL_* at redshift z'. The lensing probability is then

$$\begin{aligned}P(\mu,z;Q) \;=\; & \frac{1}{4\pi D^2(z)}\int_0^z\mathrm{d}z'\int_0^\infty dl\,(1+z')^3\,n(l,z') \\ & \times\frac{\mathrm{d}V(z')}{\mathrm{d}z}\,\sigma(\mu,z',z,l;Q)\;,\end{aligned} \tag{23}$$

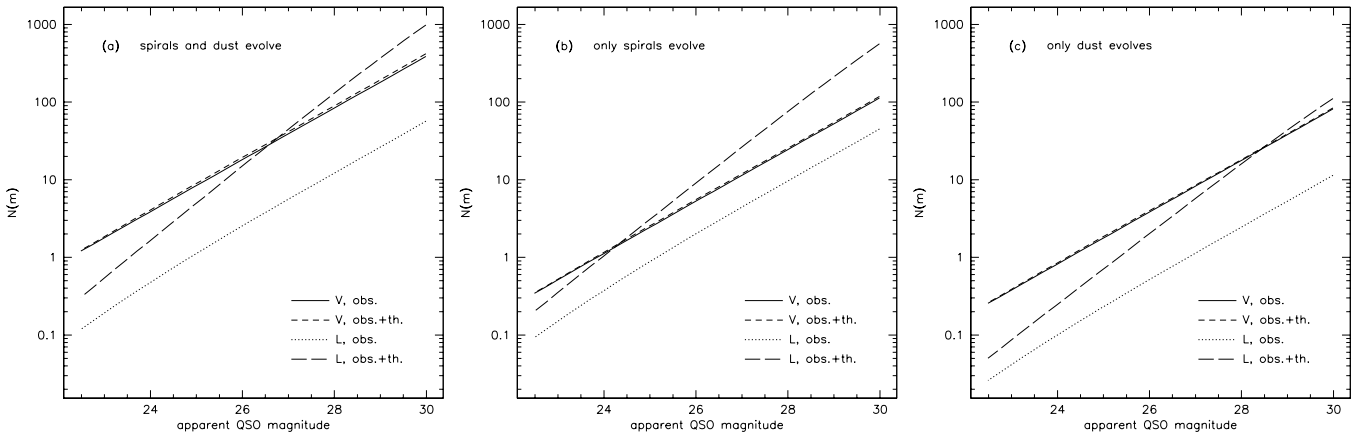

Fig. 3a–c. Number of quasars on the sky per square degree, lensed by spiral galaxies such that there are two or more images with image separation $\geq 0.1''$ and flux ratio ≤ 20. Each panel has four curves. Solid and short-dashed curves: V band, QSO luminosity function fit to the observed number counts only, or extrapolated by the theoretical model; dotted and long-dashed curve: likewise for the L band. The three panels show: **a** spiral population and dust evolve; **b** only spiral population evolves; **c** only dust evolves.

where $(1+z')^3\, n(l,z')$ is the number density of galaxies with luminosity l at redshift z', $[\mathrm{d}V(z')/\mathrm{d}z]\mathrm{d}z'$ is the proper volume of a spherical shell of width $\mathrm{d}z'$ and radius z', and $D(z)$ is the (angular-diameter) distance from the observer to the source plane.

It is important to note that total image magnifications are not only determined by lensing in our model, but also by dust extinction in the galactic disks. Total magnifications therefore range within $0 \leq \mu < \infty$ rather than $1 \leq \mu < \infty$, and therefore S' in (22) ranges within $0 \leq S' < \infty$.

The scaling relations (13) and (16) assure that the cross section σ scales with the squared Einstein radius. The Einstein radius in turn scales with the squared circular velocity, and hence with $l^{1/2}$. Assuming the scaling (16) of the disk radius, the disk parameters scale with galaxy luminosity l in the same way as the Einstein radius. This allows to immediately perform the l-integral in (23). The remaining redshift integral needs to be performed numerically.

We are left with the determination of the cross sections σ. Since the galactic disk defines a symmetry plane randomly inclined with respect to the line-of-sight, this involves averaging the cross sections over inclination angles. For fixed inclination angles, cross sections are computed by placing sources on a grid in the source plane, finding all images of each source, computing their magnifications and classifying the image properties, and finding the area in the source plane in which sources are magnified by $\geq \mu$ and imaged with properties Q.

Technically, we increase numerical efficiency by placing the sources on an adaptive grid in the source plane in order to increase numerical resolution where needed, i.e. near caustic curves. Rough image positions are then computed in a first coarse scan in the lens plane, followed by a fine scan to refine image positions and to determine accurate image properties. This technique of having adaptive grids in both the source and the lens planes increases computational speed by more than an order of magnitude compared to the straightforward fixed-grid approach. Different levels of grid refinement in the source plane are statistically accounted for by assigning appropriate statistical weights to the sources.

Having found the cross sections σ, we can evaluate the lensing probability (23). With the quasar number counts taken from Sect. 2.2, the number of quasars above flux limit S and imaged with properties Q is then computed evaluating (22).

5. Results

Multiply imaged QSOs can be recognised as such if the angular separation $\Delta\theta$ of the images exceeds a certain threshold, and if the flux ratio r between the images does not exceed a certain dynamic range. We adopt $\Delta\theta \geq 0.1''$ and $r \leq 20$ throughout this section; i.e., with "lensed QSOs" we mean multiply imaged QSOs whose images satisfy these criteria. In case of three or more images, we take $\Delta\theta$ and r between the two brightest images.

The number density of lensed QSOs per square degree on the sky is shown in Fig. 3 as a function of total apparent QSO brightness. The figure has three panels, and each panel contains four curves. Panel (a) shows results for the fiducial model. It assumes a spiral population with evolving number density and evolving disks, containing evolving dust. Dust evolution is neglected in panel (b), and the evolution of the spiral population is ignored in panel (c).

The solid and dotted curves show the number density based on the observed QSO luminosity function in the V and L bands, respectively. The L-band (dotted) curve falls below the V-band curve by approximately one order of magnitude because QSOs are intrinsically fainter in red than in blue light. The remaining two curves (short- and long-dashed) are again V- and L-band results, now based on the theoretically extrapolated QSO luminosity function by Haiman & Loeb. The changed QSO luminosity function affects the V-band counts (solid vs. short-dashed curves) only by a very small amount, while it has a very significant effect on the L-band results. The reason is the K-correction. Although the theoretically extrapolated QSO luminosity func-

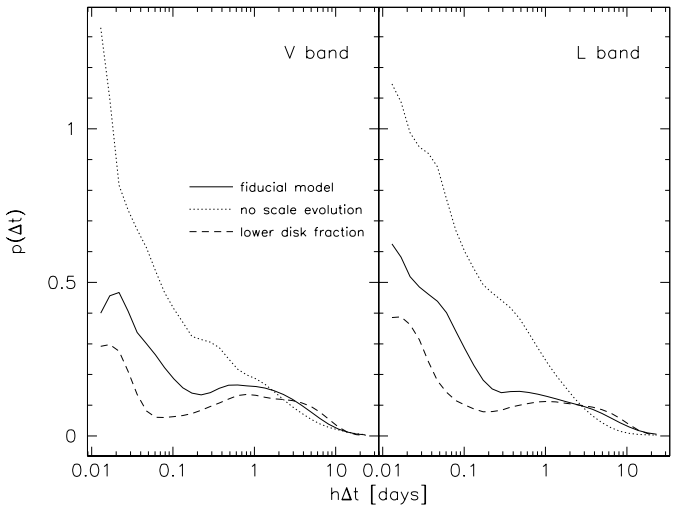

Fig. 4. Time-delay distribution for images split by $\geq 0.1''$ with flux ratio ≤ 20 and total apparent magnitude ≤ 25 in the V and L bands. Three curves are shown per panel. Solid curve: fiducial model; dotted curve: no scale evolution; dashed curve: disk fraction reduced to $f_{\rm d} = 0.5$.

tion extends to much higher redshifts than the observed one, the high-redshift QSOs are almost entirely suppressed in the V band because of the strong K-correction setting in at redshifts $\gtrsim 3.4$. In the L-band, however, the K-correction remains small or negative even at high redshifts (cf. Fig. 2). Consequently, the huge reservoir of high-redshift QSOs predicted by the theoretically modelled QSO luminosity function is not at all suppressed in the L-band, where the different assumptions for the QSO luminosity function result in number densities differing by almost one order of magnitude at apparent magnitudes of $\gtrsim 26$. Faintward of about 26.5 th magnitude, the L-band counts exceed the V-band counts.

The neglect of dust evolution in panel (b) has a strong effect on the V-band counts, and a substantially smaller effect in the L band. V-band counts are reduced by factors of $\approx 3-4$, regardless of the assumed QSO luminosity function. L-band counts based on the observed QSO luminosity function are lowered by $\approx 25\%$ compared to evolving dust, and approximately halved if the theoretically extrapolated QSO luminosity function is assumed. The reason is of course that with increasing QSO redshift, the redshift of the most efficient lenses also increases, so that QSO light in the observer's L band is more strongly affected by dust in the lenses. This leads to a relative enhancement of the L-band compared to the V-band counts.

When the spiral number density is assumed to be constant in comoving space, as in panel (c), the lensed QSO counts are reduced by almost an order of magnitude in both bands. This is due to the fact that spirals merge to form ellipticals towards redshift zero, hence the spiral number density is expected to increase towards moderate redshifts. If this increase is neglected, there are fewer lenses available and therefore fewer lensed QSOs observable.

Variation of other parameters has very little effect on the counts of lensed QSOs. Lowering the disk mass (by reducing $f_{\rm d}$ from unity to 0.5), or neglecting the expected change in spiral properties with redshift, does not change the lensed QSO counts significantly.

Fig. 4 shows the distribution of time delays between the two brightest images of lensed QSOs. The figure has two panels for the two filter bands, as indicated. Each panel shows three curves. The solid curve is the distribution for the fiducial model, in which spiral evolution is taken into account, and the disks are maximal. The curve peaks at time delays of order 0.02 days, or approximately half an hour. It goes through a local minimum at ≈ 0.2 days, and rises again for a broad and shallow peak centred on ≈ 1 day. This bimodal distribution reflects the two components of the mass distribution. Time delays of order one day occur between images whose splitting is dominated by the halo, while images straddling a near-edge-on disk have substantially smaller time delays. This is further demonstrated by changing the disk contribution to the lens model. When disk evolution is neglected, as for the dotted curve, the time-delay distribution peaks more sharply at small time delays, and the secondary maximum indicative of the halo disappears. Conversely, the secondary maximum is emphasised relative to the maximum at small time delays when the disk fraction is reduced to $f_{\rm d} = 0.5$, as for the dashed curve.

The secondary maximum in the time-delay distribution is more pronounced in the V than in the L band. The reason is the dust in the galactic disks. Images straddling near-edge-on disks, which are responsible for the peak at low time delays, are strongly suppressed by dust in the V band, but easily seen in the L band. The primary maximum in the time-delay distribution is therefore more pronounced in the L than in the V band, so that the secondary maximum is relatively lowered.

The results in Fig. 4 are based on the theoretically extrapolated QSO luminosity function, but this assumption is insignificant in this context. Adopting the observed luminosity function leads to virtually identical results.

Fig. 5 shows the fraction of multiple-image systems with three or more visible images. As before, images are considered visible if they are separated by $\geq 0.1''$ and span a dynamic range of ≤ 20. Although these systems include such with four or more images, we refer to the fraction as "triple fraction" for simplicity. The figure also has two panels for the two filter bands considered.

Both panels have four curves. The solid curve represents the fiducial model, which assumes evolution of the spirals and of the dust in the spiral disks. There are $\approx 30\%$ image systems with more than two images in the V band, and $\approx 40\%$ in the L band. It is again straightforward that there should be more such systems in the L rather than in the V band. Dust in the disks suppresses images and therefore converts part of the triple systems to doubles, and this effect is much more important in the V than in the L band.

Neglecting dust evolution leads to the dotted curves. The triple fraction is reduced to just below 10% in the V band and to $\approx 30\%$ in the L band. Obviously, the reduction compared to the model with evolving dust is more severe in the V than in the L band.

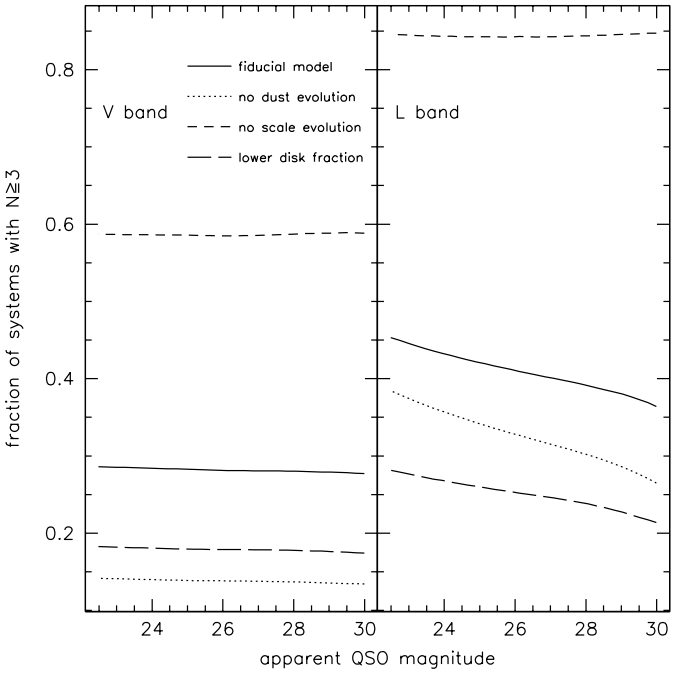

Fig. 5. Fraction of multiple image systems with three or more observable images for the V and L bands. Solid curve: fiducial model; dotted curve: no dust evolution; short-dashed curve: no scale evolution; long-dashed curve: disk fraction reduced to $f_{\rm d} = 0.5$.

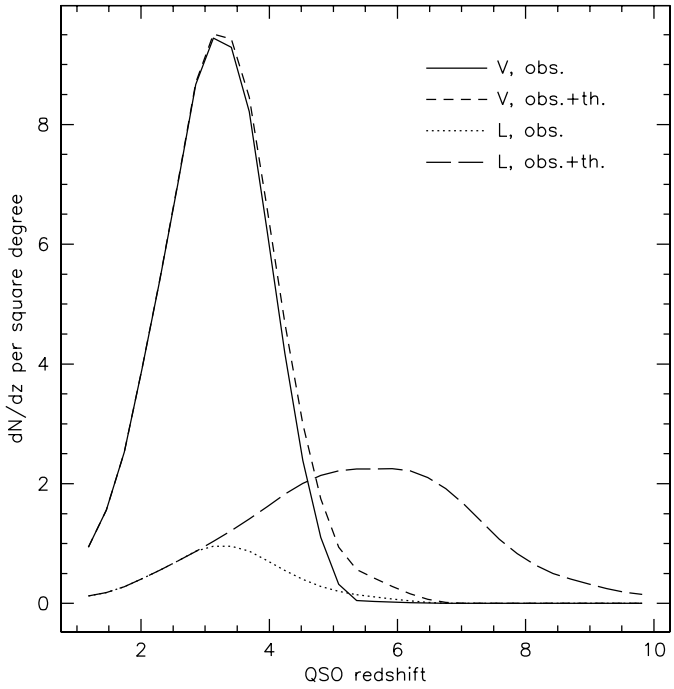

Fig. 6. Number $\mathrm{d}N/\mathrm{d}z$ of lensed QSOs with total apparent magnitude ≤ 25 per square degree and unit redshift. Solid curve: V band, observed QSO luminosity function; dotted curve: L band, observed QSO luminosity function; short-dashed and long-dashed curves: theoretically extrapolated QSO luminosity function, V and L band, respectively.

The long-dashed curves are obtained after reducing the disk fraction from unity to $f_{\rm d} = 0.5$. Generally, the triple fraction is reduced, but now the reduction is more severe in the L than in the V band. The reason for this is that dust suppresses triple systems in the V band much more strongly than in the L band. Therefore, the reservoir of triple images in the L band is much larger, so the relative effect of a lower disk fraction is stronger in the L band.

The strongest effect, however, is achieved by neglecting the evolution of spiral disks, as shown by the short-dashed curve in Fig. 5. Neglecting this aspect of the evolution leads to more extended and dominant disks at moderate redshifts. Such disks cause pronounced caustic curves with narrow, extended spikes following the projected disks. These extended caustics increase the multiple-image cross section of spirals considerably. As Fig. 5 shows, the triple fraction is increased to just below 60% in the V band, and to almost 85% in the L band.

The results shown in Fig. 5 are based on the theoretically extrapolated QSO luminosity function. Generally, the V-band results are unaffected by the choice of luminosity function, and the L-band results are generally slightly higher if the observed QSO luminosity function is used instead. The reason is highlighted by Fig. 6.

Fig. 6 shows the redshift distribution of lensed QSOs in the V and L bands which are brighter than 25 th apparent magnitude. The solid and the dotted curves show the V-band distribution with the observed and the theoretically extrapolated QSO luminosity function, respectively. The two distributions are very similar, and they peak just above $z = 3$. The distribution in the L band based on the observed QSO luminosity function (long-dashed curve) shows essentially the same behaviour, except that its amplitude is lower because of the lower L-band QSO counts at 25 th magnitude. Assuming the theoretically extrapolated QSO luminisity function, however, broadens the peak and shifts it to $z \approx 5 - 6$. The substantially higher QSO redshifts in the L band lead to more important dust extinction, and therefore to lower triple fractions, if the theoretically extrapolated QSO luminosity function is assumed.

In addition, this explains the different trends with apparent QSO magnitude of the curves in Fig. 5. While the triple fraction is essentially constant across the plotted range of magnitudes in the V band, it decreases for fainter QSOs in the L band. This is because the faint QSO population originates from a broader redshift range in the L than in the V band, and the importance of dust extinction increases with QSO redshift.

6. Conclusions

We modelled strong lensing of high-redshift QSOs by spiral galaxies, aiming at future surveys with high angular resolution and high sensitivity in a wavelength range between the visible and the near infrared. The main question was, how many multiply imaged QSOs are expected to be seen, and how do their number and their image configurations depend on the properties of the lensing spiral population?

Our mass model for the spiral galaxies consists of a spherical halo and a disk, which also contains gas and dust. The number

density of the spiral population, and the properties of spiral disks and the dust therein, are assumed to be either constant in time, or to evolve according to evolutionary models taken from the literature.

We take the observed QSO luminosity function as parameterised by Pei (1995) either as it is, or theoretically extrapolated towards high redshifts (Haiman & Loeb 1998).

We can summarise our results as follows:

1. A conservative magnitude limit above which QSO images can be distinguished against spiral disks is ≈ 26. Fainter images are expected to be visible in near-edge-on configurations.
2. At 26 th apparent magnitude, the number density of QSOs lensed by spiral galaxies reaches approximately 20 per square degree in the V band, irrespective of whether the observed or the theoretically extrapolated QSO luminosity function is assumed. The number density of lensed QSOs per square degree in the L band is ≈ 3 for the observed QSO luminosity function, and ≈ 20 for the theoretically extrapolated luminosity function. At $\mathrm{V} = 28$, the number density of lensed QSOs reaches 100 per square degree.
3. Neglecting dust evolution reduces the number density of lensed QSOs brighter than 26 th magnitude by a factor of ≈ 3 in the V band, and by a factor of ≈ 1.5 in the L band.
4. Neglecting the cosmic evolution of the spiral population reduces the number density of lensed QSOs brighter than 26 th magnitude by a factor of ≈ 5 in the V and the L bands alike.
5. The time-delay distribution peaks at small time delays below one hour. It is bimodal with a secondary maximum around one day. The short time delays are due to images straddling spiral disks, the long time delays are due to image splitting by the halo. Consequently, the secondary maximum becomes shallower or higher when the disks become more or less dominant, respectively.
6. The fraction of image systems with three or more images is of order 30% in the V band and 40% in the L band for evolving, maximal disks. It decreases when the disk fraction is reduced, and increases when the disk evolution is neglected.
7. The redshift distribution of the lensed QSOs peaks around $z \approx 3$ in the V band, regardless of the QSO luminosity function assumed. The QSO redshift distribution in the L band also peaks around $z = 3$ if the observed QSO luminosity function is assumed, but the peak broadens and shifts towards $z = 5 - 6$ for the theoretically extrapolated QSO luminosity function.

These results demonstrate that lensing of high-redshift QSOs by spiral galaxies will provide a wealth of information once an angular resolution of $\lesssim 0.1''$ can be achieved between the visible and the near infrared at flux limits of $\lesssim 26 - 28$ th magnitude. The projected NGST can reach such flux limits within at most a few minutes of exposure time. The total number of lensed QSOs per square degree reflects the number density evolution of spiral galaxies out to redshifts of $0.5 - 0.6$. The ratio of the lensed QSO number counts in the V and L bands is a measure for the dust evolution in the spiral disks. The time-delay distribution and the fraction of image systems with three or more images are sensitive to the disk mass and the scale evolution of the spiral disks.

The disks in spirals are of particular interest here. Spiral haloes alone have substantially lower lensing capabilities than ellipticals because of their lower velocity dispersions. A substantial fraction of the strong-lensing cross sections of spirals is contributed by near-edge-on disks. If they are sufficiently massive, they give rise to strongly elongated caustic curves with naked cusps. Lenses with such caustics produce characteristic image configurations, namely triple images of comparable brightness with very small angular separations straddling the disks. The occurrence and abundance of such image configurations typical for lensing by projected disks will therefore be a direct measure for the disk fraction in spirals.

Acknowledgements. It is a pleasure to thank Chris Kochanek, Avi Loeb, Paul Schechter and Peter Schneider for valuable discussions. This work was supported in part by the Sonderforschungsbereich 375 of the Deutsche Forschungsgemeinschaft.

References

Bartelmann M., Loeb A., 1998, ApJ 503, 48
Blain A.W., Møller O., Maller A.H., 1999, MNRAS 303, 423
Brocklehurst M., 1971, MNRAS 153, 471
Broeils A.H., van Woerden H., 1994, A&AS 107, 129
Coleman G.D., Wu C.-C., Weedman D.W., 1980, ApJS 43, 393
Draine B.T., Lee H.M., 1984, ApJ 285, 89
Eke V.R., Cole S., Frenk C.S., 1996, MNRAS 282, 263
Elvis M., Wilkes B.J., McDowell J.C., et al., 1994, ApJS 95, 1
Falco E.E., Kochanek C.S., Muñoz J.A., 1998, ApJ 494, 47
Freeman K.C., 1970, ApJ 160, 811
Fukugita M., Turner E.L., 1991, MNRAS 253, 99
Grandi S.A., 1981, ApJ 251, 451
Grandi S.A., 1982, ApJ 255, 25
Guiderdoni B., Rocca-Volmerange B., 1988, A&AS 74, 184
Haiman Z., Loeb A., 1998, ApJ 503, 505
Haiman Z., Loeb A., 1999, In: Holt S., Smith E. (eds.) After the Dark Ages: When Galaxies were Young. Proc. 9th Annual October Astrophysics Conference in Maryland. AIP Press (preprint astro-ph/9811395)
Keeton C.R., Kochanek C.S., 1998, ApJ 495, 157
Keeton C.R., Kochanek C.S., Seljak U., 1997, ApJ 482, 604
Keeton C.R., Kochanek C.S., Falco E.E., 1998, ApJ 509, 561
Kochanek C.S., 1996a, ApJ 466, 638
Kochanek C.S., 1996b, ApJ 473, 595
Kochanek C.S., Falco E.E., Impey C.D., et al., 1999, In: Holt S., Smith E. (eds.) After the Dark Ages: When Galaxies were Young. Proc. 9th Annual October Astrophysics Conference in Maryland. AIP Press (preprint astro-ph/9811395)
Magorrian J., Tremaine S., Richstone D., et al., 1998, AJ 115, 2285
Maller A.H., Flores R.A., Primack J.R., 1997, ApJ 486, 681
Maoz D., Rix H.-W., 1993, ApJ 416, 425
Marzke R.O., Geller M.J., Huchra J.P., Corwin H.G., 1994, AJ 108, 437
Mo H.J., Mao S., White S.D.M., 1998, MNRAS 295, 319
Murdoch H.S., Hunstead R.W., Pettini M., Blades J.C., 1986, ApJ 309, 19

Netzer H., Davidson K., 1979, MNRAS 187, 871
Pei Y.C., 1995, ApJ 438, 632
Pei Y.C., Fall S.M., Bechtold J., 1991, ApJ 378, 6
Press W.H., Schechter P., 1974, ApJ 187, 425
Rocca-Volmerange B., Guiderdoni B., 1988, A&AS 75, 93
Sasaki S., 1994, PASJ 46, 427
Schechter P., 1976, ApJ 203, 297
Schade D., Carlberg R.G., Yee H.K.C., López-Cruz O., 1996, ApJ 465, L103
Spitzer Jr. L., Greenstein J.L., 1951, ApJ 114, 407
Tully R.B., Fisher J.R., 1977, A&A 54, 661
Turner E.L., Ostriker J.P., Gott III J.R., 1984, ApJ 284, 1
Van der Marel R.P., 1999, AJ 117, 744
Viana P.T.P., Liddle A.R., 1996, MNRAS 281, 323
Whittet D.C.B., 1992, Dust in the Galactic Environment. Hilger, Philadelphia